Environmental Technology & Innovation 28 (2022) 102866

Contents lists available at ScienceDirect

Environmental Technology & Innovation

journal homepage: www.elsevier.com/locate/eti

Carbon-covered alumina-supported ZnO nanocatalysts with enhanced visible light photocatalytic performance for the removal of dyes

Abayomi D. Folawewo, Muhammad D. Bala [*]

School of Chemistry & Physics, University of KwaZulu-Natal, Westville Campus, Private Bag X54001, Durban 4000, South Africa

ARTICLE INFO

Article history:
Received 28 May 2022
Received in revised form 2 August 2022
Accepted 4 August 2022
Available online 11 August 2022

Keywords:
Carbon-covered alumina
ZnO
Azo dyes
Nanocatalyst
Wastewater purification

ABSTRACT

In this study, environmentally sustainable catalysts were prepared economically as a positive step in directly using visible light to degrade wastewater polluted with industrial dyes. Hence, zinc oxide (ZnO) nanocatalysts doped with carbon-covered alumina (CCA) were fabricated by the sol–gel technique using zinc acetate as the precursor and CCA as the support. Various methods were used to characterize the catalysts, including XRD, TEM, EDS-SEM UV/Vis-DRS, EIS, PL, and BET. The new CCA-supported catalysts are crystalline with high surface areas. The photocatalytic capability of the catalysts was studied using azo dyes as model pollutants. Hence, sunset yellow and tartrazine were degraded up to 99% by the catalysts, which were also recycled five times without loss in activity. Details on the kinetics and mechanistic mode of catalyst action are presented and analysed. Chemical oxygen demand measurements further confirmed the mineralization of the dyes. The study showed that the ZnO/CCA/Vis photocatalysis has good prospects of adoption for large-scale pre-treatment of dye-polluted wastewaters. This technique is suited to the food, textile and allied industries that employ substantial quantities of colourants.

1. Introduction

Many industrial applications that use large quantities of colourants, including textiles, tanning, paper, food, photoelectrochemical cells, pharmaceuticals and light-harvesting arrays, are sources of contamination of water resources (Ajmal et al., 2014; Crini, 2006; Dixit et al., 2015; Hasanbeigi and Price, 2015; Perez-Urquiza and Beltran, 2000; Wróbel et al., 2001; Yang et al., 2008). All these industries use massive amounts of water and discharge harmful chemicals as effluents, including coloured dyes, causing an imbalance in the ecosystems of water bodies by way of visual contamination, eutrophication, and distress to the living organisms (Ajmal et al., 2014). It is essential to highlight that most dyes contain toxic organic compounds (Konstantinou and Albanis, 2004), and approximately 50%–70% of the dyes on sale today are azo (–N=N–) compounds. Increased exposure to high levels of azo dyes by humans may put the body at risk of serious diseases such as infertility, thyroid cancer, asthma, migraines, eczema and autoimmune diseases (Caliman et al., 2008). As a result, decolourizing dye effluents before discharge to waterways has gained more attention from scientists and policymakers. One commonly adopted technique involves using heterogeneous (semiconductor) photocatalysis. It is an emerging technology with the benefit of in-built destructive characteristics for mineralizing organic compounds under

---

[*] Corresponding author.
E-mail address: bala@ukzn.ac.za (M.D. Bala).

https://doi.org/10.1016/j.eti.2022.102866

UV irradiation (Serrà et al., 2019; Zhang et al., 2019). Also, it is not mass transfer limited and can be done under ambient settings (with atmospheric oxygen as an oxidant). It also completely mineralizes the pollutant carbon into CO_2 and other harmless products. In this regard, zinc oxide (ZnO) has attracted much attention as a 'future semiconductor' and is extensively investigated as a photocatalyst material for removing organic compounds from contaminated water (by advanced oxidation processes) (Chen et al., 2017; Quraishi et al., 2020). More importantly, ZnO is resistant to photo corrosion, chemically stable, non-toxic, cheap and capable of producing many reactive radicals that can destroy organic functional groups (Ranau and Steinhart, 2004). ZnO is a wide bandgap semiconductor (3.3 eV) with high exciton binding energy (∼60 eV), which ensures efficient excitonic UV emission at ambient temperatures (Afzaal et al., 2007). However, the enormous bandgap energy in the UV spectrum reduces its use on exposure to natural sunlight (which contains 43% visible light and only 4% UV), and a high recombination rate of the charge carriers are the primary issues, restricting its large-scale usage (Sarmah et al., 2018). In addition, UV light is expensive and not commercially viable due to high energy usage, and in large doses, it is also harmful (González-Casamachin et al., 2019). Hence, much study has been undertaken to develop visible-light photocatalysts built around modified ZnO to overcome these restrictions. These include using binary or ternary semiconductors and various doping strategies (transition metal and nonmetal dopants) to produce modified ZnO nanocatalysts. Also, the nanocatalysts are implanted on a variety of supports (activated carbon, graphite, carbon-covered alumina (CCA) (Mahlambi et al., 2012), and carbon nanotubes (Moradi et al., 2017) to improve photocatalytic activity and recovery from aqueous media.

Carbon and alumina are the most commonly used anchor or support materials. However, using a single material as support has several drawbacks; for instance, although a support material like γ-alumina has many pores that can disperse the active metal phase, good mechanical properties and a high surface area when it is used alone, its acidity causes low catalytic activity (Zheng et al., 2008). This is because acidic metal oxides form on its reactive surfaces upon calcination (due to the interaction of alumina with promoter ions like Co^{3+} and Ni^{2+}). On the other hand, carbon supports have attractive properties like good conductivity, high surface area and a tunable pore volume. Carbon also has a variable surface functional group and resists nitrogen poisoning (Boorman et al., 1991). However, like alumina, it exhibits poor mechanical strength when used as the sole support material; it easily disintegrates and has a low bulk density. Also, a catalyst may be deposited in its pores because it is microporous, undermining its activity (Boorman et al., 1991). Hence, CCA as a hybrid support material circumvents the shortcomings of alumina and carbon.

Recently, CCA has been used as a support for hydrotreating catalysts and ammonia synthesis (Maity et al., 2009; Masthan et al., 1991). It has also been modified into various forms for different applications (Jana and Ganesan, 2011), but CCA-based catalysts have rarely been employed in wastewater clean-up. A review of current literature shows that a silver nanocatalyst has been anchored on CCA to screen microbes in drinking water (Shashikala et al., 2007). Also, CCA-TiO_2 and metal-TiO_2 on CCA (Mahlambi et al., 2012, 2013) materials have been used to remove Rhodamine B dye on exposure to visible light.

Hence, the objectives of this research include: (i) the use of CCA as a support material; aimed at reducing the recombination rate of the charge carriers (e^-/h^+) by modulating the activity of the ZnO catalysts, (ii) improving the recovery and reusability of the catalysts with robust support, and (iii) expanding the optical absorbance band of the ZnO catalysts into the visible light region thus, improving and simplifying overall photocatalytic activity. In addition, the novelty of this work includes developing ZnO-based composite materials with improved light absorption in the visible region. This was achieved by supporting ZnO semiconductors onto CCA economically and sustainably. In addition, the developed catalysts were effective for wastewater purification by visible light irradiation. Finally, the CCA reported in this project is robust enough to support improved catalyst recyclability and enhanced visible light sensitization of the dye substrates (Bond and Bergstrom, 2006; Mahlambi et al., 2012; Lin et al., 2005). To the best of our knowledge, this report is the first instance where ZnO nanocatalysts are supported on CCA for the photochemical treatment of azo dyes in wastewater.

2. Materials and methods

2.1. Materials

All reagents were of analytical grade. Zinc acetate, calcium hydride, and oxalic acid were purchased from Industrial Analytical (South Africa). Absolute ethanol (EtOH), tartrazine, and sunset yellow (FCF) dyes were supplied by Capital Research Distributor Co., Ltd (South Africa). Sulphuric acid (98%), γ-alumina (calcined at 500 °C for 3 h to remove any organic impurities), disodium ethylenediaminetetraacetic acid (EDTA), n-xylene (dried over calcium hydride overnight before usage), p-benzoquinone (BQ) and toluene 2,4-diisocyanate (TDI, used without purification) were purchased from Merck (Pty) Ltd (South Africa). Analytical grade n-propanol and Isopropyl alcohol (IPA) were purchased from Industrial Analytical (Pty) Ltd (South Africa). The IPA was distilled before usage.

2.2. Preparation of ZnO

ZnO was prepared by the sol–gel method. A solution (A) was formed from 0.01 mol of zinc acetate dissolved in 60 mL of EtOH at 60 °C and stirred for 30 min. Solution B was made by dissolving 0.02 mol of oxalic acid dihydrate in 80 mL of EtOH at 50 °C and stirring for 30 min. Solution B was added dropwise to warm solution A and stirred continuously for 1 h. A white sol was obtained, aged, and dried for a day at 80 °C, then treated at 450 °C to produce the ZnO (Chen et al., 2017).

2.3. Preparation of carbon-covered alumina support

The CCA support was prepared by modifying the adsorption–pyrolysis method. A blend of γ-alumina (5 g) and 1% TDI in n-xylene (115 mL) were stirred at ambient temperature for 24 h. The resulting mixture was filtered and washed severally with n-xylene (100 mL). A feathery white precipitate was obtained and dried overnight at 80 °C. The precipitate obtained was then pulverized and placed into a quartz cell. The temperature was gradually increased to 700 °C under a nitrogen flow (30 mL/min) and held at the same temperature for 3 h to complete the pyrolysis of the TDI (Sharanda et al., 2006).

2.4. Preparation of carbon-covered alumina-ZnO nanocatalysts

A colloidal suspension of 100 mg of ZnO in 30 mL deionized water was prepared and sonicated for 30 min at ambient temperature, followed by adding 100 mg of the prepared CCA, sonicated for 1 h and left at ambient temperature for 24 h to dry. The resulting product was dried at 80 °C overnight to yield the ZnO/CCA (1:1), which was then pulverized and treated at 450 °C for 3 h to afford the ZnO-impregnated on the CCA support. The same procedure was used to prepare the ZnO/CCA (2:1) and (1:2) nanocatalysts, with the two materials' relative ratios adjusted accordingly.

2.5. Chemical oxygen demand (COD) analysis

COD analysis was determined using COD vials purchased from Merck Inc. South Africa (COD Cell Test 10–150 mg/L with product number: 1.14540.001). COD is generally used to determine the content of oxidizable organic matter in a wastewater sample. For this, 3 ml of the sample wastewater was dispersed into the COD vials and vortexed for 2–3 min to ensure thorough sample mixing with the COD reagents. The sample was then digested in a thermoreactor at 148 °C for 2 h and allowed to cool down before determining the value of the COD. The control cuvette was used to zero the instrument. The test results were expressed as mg/L COD, and COD per cent reduction was calculated using Eq. (1) (Morshed et al., 2019).

$$\mathrm{COD}\ (\%) = \frac{\mathrm{COD_0} - \mathrm{COD_t}}{\mathrm{COD_0}} \times 100 \tag{1}$$

Where $\mathrm{COD_0}$ and $\mathrm{COD_t}$ are the initial COD and COD at time t, respectively.

2.6. XRD analysis

The crystalline nature and the final phase of the product were studied by powder X-ray diffraction (PXRD). The PXRD measurements were performed using a Bruker D8-Advance diffractometer (Bruker AXS — Germany) operated in a continuous θ–θ scan in locked coupled mode with Cu-K_α radiation. The measurement was determined within the range of 2θ as required by the user with a step size of 0.034° in 2θ ($\lambda K\alpha_1 = 1.5406$ Å). A position-sensitive detector, Lyn-Eye, was used to acquire the diffraction data at a speed of 0.5 s/step, corresponding to an effective 92 s/step time for a scintillation counter. The shape factor k was used to correlate the size, and the Debye–Scherrer equation, $D = K\lambda/\beta \cos\theta$, was used to estimate the crystallite size, where the constant $k = 0.9$, $\lambda = 1.54060$ Å is the X-ray wavelength, β is the full width half maximum (FWHM) of the catalyst, and θ is the diffracting angle (radians). The Miller planes of all the prepared samples were confirmed using JCPDS XRD library software.

2.7. Brunauer–Emmett–Teller (BET) measurements

A Micromeritics TriStar II (USA) surface area and porosity analyzer was used to measure all prepared samples' surface areas (SBET), pore-volume, and pore size distributions. Each sample was degassed in N_2 under vacuum for 24 h at 200 °C before analysis. Each sample was heated to 90 °C at a heating rate of 5 °C/min and held at the same temperature for 180 min, then evacuated at a pressure of 50 mmHg for 30 min. The temperature was gradually raised to 180 °C at a heating rate of 10 °C/min and degassed 24 h under N_2.

2.8. SEM, TEM, and EDX spectroscopy

The structure and morphology of the nanocatalysts were studied using a Carl Zeiss Ultra Plus FEG (ZEISS, Germany) fitted with an energy dispersive Oxford X-max detector (Oxford Instruments, UK) operating at a voltage of 30 kV for scanning electron microscopy (SEM) and JEOL 2100 (JEOL Ltd, Japan) operating at both standard and high-resolution modes at an operating voltage of 200 kV for transmission electron microscopy (HR-TEM) JEOL 2100 (JEOL Ltd, Japan). First, before imaging, the samples were dispersed in EtOH and sonicated, and then the sample holder was immersed in the suspension. The sample holder was dried under UV light before reinsertion into the TEM sample port for imaging. The SEM and TEM were equipped with an EDX detector for qualitative analysis of all the prepared samples.

2.9. Photoluminescence (PL)

Photoluminescence (PL) spectra were acquired using a PerkinElmer LS 55 (USA) spectrofluorimeter using an excitation wavelength of 350 nm and emission slit widths of 10 nm. About 5–10 mg of the sample was placed in a sample holder, and the PL spectra were then acquired in the 390–800 nm wavelength range.

2.10. UV–Visible by solid-state diffuse reflectance spectra (UV-DRS)

UV/Vis reflectance spectra were acquired using a PerkinElmer Lambda 35 (USA) UV–Vis spectrophotometer fitted with a Labsphere integrating sphere (Labsphere, USA). Using the corresponding Kubelka–Munk functions (F(R)), the bandgap energy was calculated by plotting $(F(R)\text{-}hv)^2$ against $h\nu$.

2.11. Fourier transform infrared (FTIR)

FTIR spectra were recorded on a PerkinElmer Spectrum 100 spectrophotometer (USA) equipped with an attenuated total reflectance (ATR) sampling accessory. All spectra were acquired in the transmission mode in the 500–4000 cm^{-1} range, with 32 scans and a resolution of 2.0 cm.

2.12. Thermogravimetric analysis (TGA)

The thermal stability of the samples was determined with a Thermogravimetric Analyzer with a small furnace (SF) (Mettler Toledo, Germany). The TGA was measured at a heating rate of 10 °C/min from 25 to 800 °C in air.

2.13. Electrochemical analysis

The photocurrent response of the samples was investigated using electrochemical analysis. This is to evaluate charge carrier separation efficiency during photocatalysis. Hence, measurements were carried out on a VersaSTAT 3F electrochemistry workstation (AMETEK Scientific Instruments, USA). A three-electrode set-up was used, with a reference (Ag/AgCl), counter (platinum wire), and a working electrode with 0.5 M Na_2SO_4 as electrolyte. The working electrode was made by modifying glassy carbon electrodes (GCE) with the appropriate photocatalysts (prepared samples). For the modification, 10 mg of the sample and 3 mg of carbon paste (binder) were dispersed in EtOH and sonicated for 30 min. The suspension was drop-cast onto a clean, glassy carbon electrode with a micro-pipette and dried overnight. The set-up was flushed with N_2 gas for 5 min to remove dissolved oxygen from the suspension, which would affect the system. The electrochemical impedance spectroscopy (EIS) measurements were performed using the three-electrode system (Yang et al., 2021).

2.14. Set-up for photocatalytic reactions

A commercial fluorescent lamp (3U E27 32w, cool white, 8000 h) with an optical filter to cut-off UV light was used in a closed photocatalytic chamber for the photocatalytic reactions. The light intensity at the reaction position is 880 W/m^2 without a filter and 830 W/m^2 with the UV cut-off filter ($\lambda > 420$ nm). An Oriel 70260 Radiant Power meter was used to measure the intensities. The distance between the light and the reactor is 10 cm. The photocatalytic properties of the catalysts were determined on 100 mL (20 mg/L) dye samples. The prepared nanocomposites (10 mg per 100 mL of 20 mg/L dye) were used in the suspension. The set-up was agitated over an electric stirrer for 30 min before exposure to the lamp to balance adsorption–desorption between the dye and the nanocatalyst. Aliquots of 4 mL were collected from the reactor at 15 min intervals to determine the amount of dye removed. The sample was centrifuged at 6000 rpm for 15 min before absorbance measurement, and the supernatant was filtered via a 0.45 μm microfilter to remove the catalyst. The absorbance of the filtrate was measured at a λ_{max} of 482 and 427 nm for sunset yellow (FCF) and tartrazine, respectively. Eq. (2) was used to compute the percentage removal of dyes over time. The set-up was the same for both ZnO and ZnO/CCA (1:2) nanocomposite.

$$\left(\frac{A_0 - A_t}{A_0}\right) \times 100\% \tag{2}$$

Where A_0 is the original absorbance of the dye before exposure to visible light, and A_t is the absorbance of the dye at time t. For the recyclability test, the best catalyst was recovered, and the procedure described was repeated under the same settings for four more catalytic runs to study its stability.

3. Results and discussion

3.1. Structural properties

The chemical structures of the mono azo anionic dyes, sunset yellow and tartrazine used as model compounds for the study are presented in Table 1, with the functional azo bond highlighted.

Table 1
Chemical structures of the anionic mono azo dyes.

Azo dyes	Structure	Formula	Molecular weight (g/mol)
Sunset yellow (FCF)	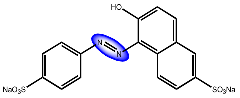	$C_{16}H_{10}N_2Na_2O_7S_2$	452.36
Tartrazine	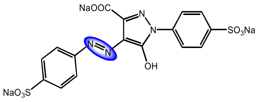	$C_{16}H_9N_4Na_9S_2$	534.36

Table 2
Structural and textural properties of the ZnO/CCA samples.

Entry	Sample	Crystallite size (nm)	S_{BET} (m^2/g)	Pore volume (m^3/g)	Pore size (nm)
1	Alumina	2.62	202.55	0.387	6.27
2	CCA	2.55	144.62	0.297	6.50
3	ZnO	15.52	13.78	0.259	4.30
4	ZnO/CCA (1:2)	17.19	110.91	0.387	6.27

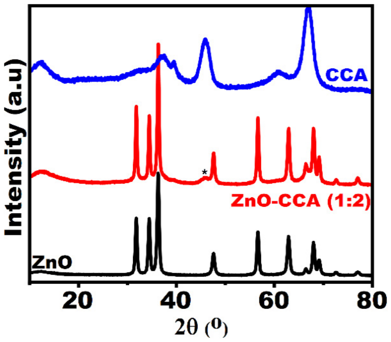

Fig. 1. Powder X-ray diffraction patterns of ZnO, CCA and ZnO/CCA (1:2).

3.1.1. *XRD analysis*

A stack of the PXRD diffractograms of the catalyst materials is presented in Fig. 1. The pattern of the diffractogram of the CCA support did not show any peaks related to ordered carbon structures, indicating that C is in the amorphous form or it is a thin graphitic layer in the CCA (Liu, 2011; Sharanda et al., 2006). XRD can only identify graphite loads with a height of at least 3 nm, corresponding to approximately 10 layered graphene sheets. In the case of the CCA sample, it appears that highly defective and nanosized carbon particles were present (Kazakova et al., 2021; Mendes et al., 2020; Sun et al., 2020). However, the CCA displayed peaks linked to alumina at $2\theta = 32.61$ (220), 37.28 (311), 39.50 (222), 45.93 (400), 60.66 (333), and 66.92° (440), which correspond to the PXRD data obtained from the JCPDS card no 00-047-1308.

The signal observed at 45.86° in the spectra of CCA and CCA-ZnO (1:2) (labelled '*') is indicative of the formation of the ZnO/CCA (1:2) composite. The diffractogram of pure ZnO revealed characteristic sharp and well-defined signals at $2\theta = 31.77$, 34.38, 36.29, 47.59, 56.63, 62.88, 66.37, 67.99, and 69.15°. The corresponding miller indices [(100), (002), (101), (102), (110), (103), (200), (112) and (201)] confirm the presence of a wurtzite hexagonal structure of the ZnO with the preferred (101) plane (JCPDS no. 00-036-1451; a = b = 3.24982 Å, c = 5.20661 Å; space group; P63mc). As seen in Fig. 1, no impurity peaks were observed, indicating that the ZnO/CCA composite is phase pure. This shows that embedding ZnO on the CCA had no negative effects on the photocatalyst core (degree of crystallinity) or the CCA support. The average crystallite size of the prepared samples was calculated (Debye–Scherrer equation) as 15.52 and 17.19 nm for ZnO and ZnO/CCA (1:2), respectively. Furthermore, the crystallinity indexes for the ZnO and ZnO/CCA are 85% and 83%, respectively. The values suggest that the CCA support had little impact on catalyst crystallinity. The average crystallite size of ZnO is in close agreement with reported literature data (Ong et al., 2016). In addition, the interlayer spacing was estimated at 0.220 nm for the ZnO/CCA (1:2).

3.1.2. *Surface area and porosity*

The efficiency of a photocatalyst is determined by its surface area, pore volume, and pore size distribution (porosity). Nitrogen (N_2) adsorption–desorption isotherms at 77 K were used to calculate the surface area (BET) and porosity (BJH). The BET isotherms of all the prepared samples with the pore size distribution plot as insets are presented in Fig. 2 and ESI Fig. S1, while the key data are summarized in Table 2.

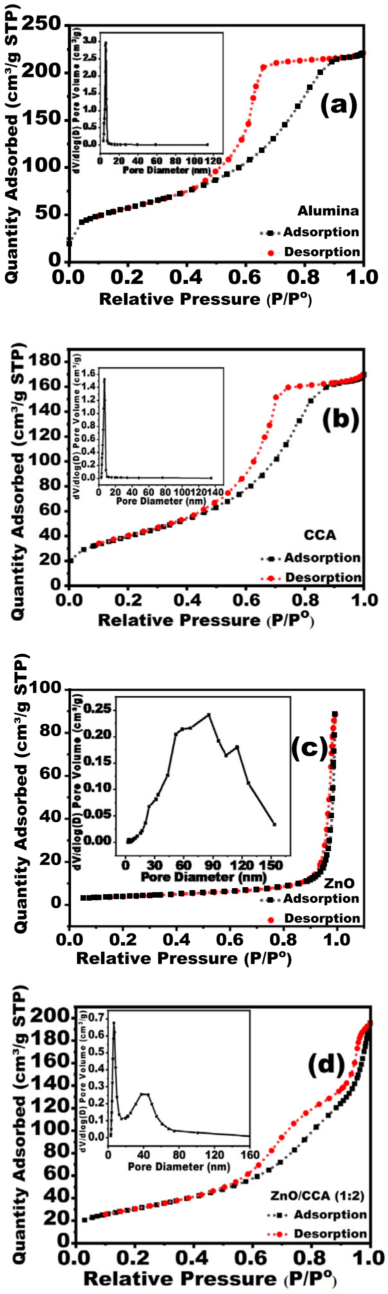

Fig. 2. BET isotherms and the BJH pore volumes of (a) γ-alumina, (b) CCA, (c) ZnO, and (d) ZnO/CCA (1:2).

The data shows the effects of carbon loading on the surface of alumina and the influence of embedding the ZnO nanocatalysts on the CCA. It is noted that alumina, CCA, and ZnO/CCA (1:2) possess a heterogeneous pore structure and exhibited the adsorption–desorption isotherms classified as type IV based on the BET classification, indicating their mesoporous nature. It is noteworthy that the surface interactions between the adsorbent and the adsorbate determine the adsorptive nature of mesoporous materials. These interactions are directed by intermolecular forces in the condensed state with features that include pore condensation, a process whereby a gas condenses into a liquid-like phase in a pore at a pressure P less than the saturation pressure P_0 of the bulk liquid (Landers et al., 2013; Monson, 2012). ZnO exhibited a hysteresis loop of type H3 associated with capillary condensation and multilayer adsorption on the surface of the nanocatalyst. Its structure allows the dispersion of pollutants through the mesoporous channels to be destroyed on the catalyst surface. All the samples showed large hysteresis loops, with alumina having the largest one at $P/P_0 = 0.4$–0.9, signifying that it is relatively more mesoporous with a good adsorption capacity ($\sim$219 cc/g at $P/P_0 = 1$). This is in comparison to CCA (∼170 cc/g at $P/P_0 = 1$) and ZnO/CCA (∼197 cc/g at $P/P_0 = 1$). After impregnation, the ZnO/CCA (1:2) formed exhibited a type H2 hysteresis loop (at $P/P_0 = 0.5–1.0$). This type of isotherm describes the process of nitrogen adsorption on the adsorbent surface. Also, this type is associated with a sharp desorption branch at a relative pressure close to the lower end of hysteresis (adsorption–desorption). The steep desorption observed in H2 loops can be ascribed to either pore-blocking/percolation in a narrow range of pore necks or cavitation-induced evaporation. It has channel-like pores with non-uniform pore size distribution within the mesoporous regions (2–50 nm pore diameter) (Nishikiori et al., 2012) according to the BET grouping (Sing, 1985; Thommes et al., 2015).

Additionally, the ZnO exhibited an active area value of 13.78 m^2/g. In contrast, the CCA was determined as 144.62 m^2/g, which is in close agreement with previously reported values (Kazakova et al., 2021; Mendes et al., 2020; Souza Macedo et al., 2019). In comparison, ZnO/CCA (1:2) exhibited a 110.91 m^2/g surface area, which is larger and better with more active reaction sites that may accelerate the separation efficiency of photogenerated carriers. These results suggest that some micropores of the CCA were locked (blocked) by the introduction of ZnO into the composite. This observation agrees well with previous work (Lin et al., 2019; Solodovnichenko et al., 2019). Table 2 shows the textural features of the most active of the prepared samples. The increase in the active area of the ZnO/CCA (1:2) compared to pure ZnO was due to carbon loading, which agrees with a previous study (Mahlambi et al., 2012). Hence, increase in the available active area for dye adsorption and removal. Additionally, embedding the semiconductor onto CCA resulted in little change in the pore volume (Legrand et al., 2021; Lin et al., 2019).

3.2. Morphological studies

3.2.1. SEM, TEM, and EDX spectroscopy

The surface structure and nature of the prepared samples were studied by scanning electron microscopy (SEM), transmission electron microscopy (TEM), high resolution-transmission electron microscopy (HR-TEM), and energy dispersive X-ray analysis (EDS). The data is presented in Figs. 3–4.

Analysis of the SEM image of alumina (Fig. 3a) shows that it contains lumpy particles with a coarse surface and size distribution of 21–23 nm. In contrast, the CCA surface seen in Fig. 3(b) is relatively smooth due to the homogeneous covering of carbon. Also, the surface of the CCA support appears porous and thus offers a larger specific area for supporting the catalyst. The SEM image of ZnO showed spherical particles, but the agglomeration of the particles was high due to calcination (Behnajady et al., 2011; Bekele et al., 2021). Fig. 3(d) represents the hybrid combination of the ZnO catalyst on the CCA surface with a particle size distribution in the 21–25 nm range. The ZnO catalyst appears set in the pores of the CCA, implying that it can be used in catalysis without unravelling from the support.

The microstructure of the ZnO/CCA (1:2) catalyst was further investigated by TEM. The TEM image of alumina revealed a rough surface (Fig. 4a), and the image of pure ZnO displayed a spherical morphology as reported by others (Idriss et al., 2017; Oprea et al., 2011; Ribut et al., 2018). This is shown in Fig. 4b with a highlight of the typical crystalline ZnO hexagonal wurtzite structure. Also, Fig. 4c displayed the TEM image of the CCA support, which shows that it is microporous and fluffy due to the carbon covering. It is well understood that ideal graphene has a triangular sublattice of equivalent carbon atoms. However, the sublattice composition of defective graphene may differ, resulting in corresponding changes in the carbon content of the monolayer coating of disordered carbon as observed in the TEM image (Fig. 4c), which is also confirmed by XRD analysis (see ESI Fig. S2c) (Kazakova et al., 2021). In addition, Fig. 4d displays the TEM image of ZnO (embedded on CCA), seen as dark spots (Mahlambi et al., 2013; Xue et al., 2015). The TEM image shows the supported ZnO nanocomposite as a crystalline material (crystallinity index of 83%). Hence, we reason that the CCA will enhance its performance as a catalyst. This is further supported by the corresponding SAED pattern (Fig. 4e), which shows a set of concentric rings as clear evidence of polycrystalline nanocomposite material. It is made up of the many crystallites that appear as the discrete spots on the rings, which arise from Bragg's reflections (compare with the SAED patterns of the prepared ZnO and CCA — ESI Fig. S2). The interlayer spacing was determined as 0.284 nm in the ZnO/CCA (Fig. 4f), which agree well with the XRD data (0.220 nm).

The elemental composition of the prepared nanocomposites was analysed using EDX (ESI Fig. S2), which showed that the required elements (Al, O, C and Zn) are all present in the samples. Each nanocomposite sample is constituted as required, which serves as further evidence for the formation of the ZnO/CCA (1:2).

3.3. Optical properties

3.3.1. Photoluminescence (PL) analysis

Room-temperature PL emission of the ZnO and the various ZnO/CCA composites was studied to gain insight into the charge transfer capacity of the as-prepared catalysts. This is essential because their photocatalytic performance is primarily determined by the generation, transfer and recombination of photogenerated e^-/h^+ charges. The data [excitation wavelength of 350 nm] presented in Fig. 5 is critical for understanding the photocatalytic performance of the catalysts.

Typically, there are two emission bands in a PL spectrum. The near band edge (NBE) excitonic UV emission and deep-level emission in the visible spectrum (Wang et al., 2003; Zhou et al., 2007). Recombination of the charge carriers (e^-/h^+ pair) inside the material releases radiation as PL. A ZnO semiconductor exhibits wide bandgap energy at room temperature with a large exciton binding energy and an emission in the UV/Vis region of the spectrum, as seen in Fig. 5 (Hu and Bando,

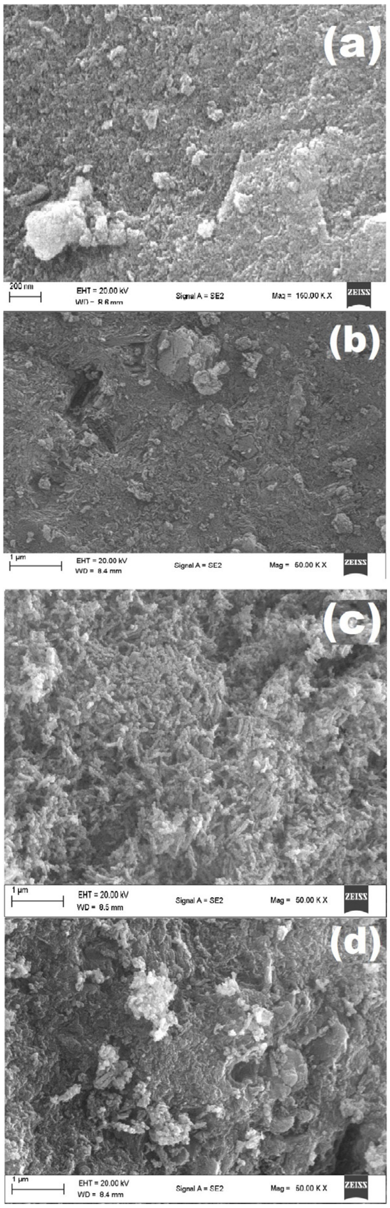

Fig. 3. SEM micrographs for (a) alumina, (b) CCA, (c) ZnO and (d) ZnO/CCA (1:2).

2003). From the PL data for all the synthesized catalysts, the NBE excitonic UV emissions are located at 394 nm for ZnO, 415 nm for ZnO/CCA (1:1), 420 nm for ZnO/CCA (2:1), and 421 nm for ZnO/CCA (1:2). These values agree well with the bandgap energies obtained by the DRS study. The emission spectral peaks in the visible region for all the ZnO-modified nanocatalysts are weak and broad. In addition, the deep-level emissions are located at 482–525 nm in the visible region for all the samples. The signal at 482 nm (blue region) can be ascribed to the electronic transition from the shallow donor level of zinc interstitial defects to the valence band and the transition of electrons from the conduction band to the singly ionized zinc vacancy ($V_{\mathrm{Zn}-}$) (Kandula and Jeevanandam, 2014). In comparison, the signal at 525 nm (green region) is due to the trapping of electrons in the defect energy level corresponding to oxygen vacancy (V_0), which controls the recombination of electrons and holes (Ischenko et al., 2005; Nadupalli et al., 2021). The observed increase in the PL intensity for the ZnO/CCA (2:1) system is due to the high recombination rate of the charge carriers. This could be a result of inadequate charge separation (less than optimum CCA content in the sample). Moreover, the recombination rate is higher than that of pure ZnO. However, the weaker PL peak intensity of the ZnO/CCA (1:2) sample alludes to the effective separation of charge carriers. The reduction in the PL intensity of the ZnO/CCA (1:2) sample is due to incorporating an optimum amount of ZnO onto an adequate amount of CCA. This confirms the decrease in the bandgap energy of the

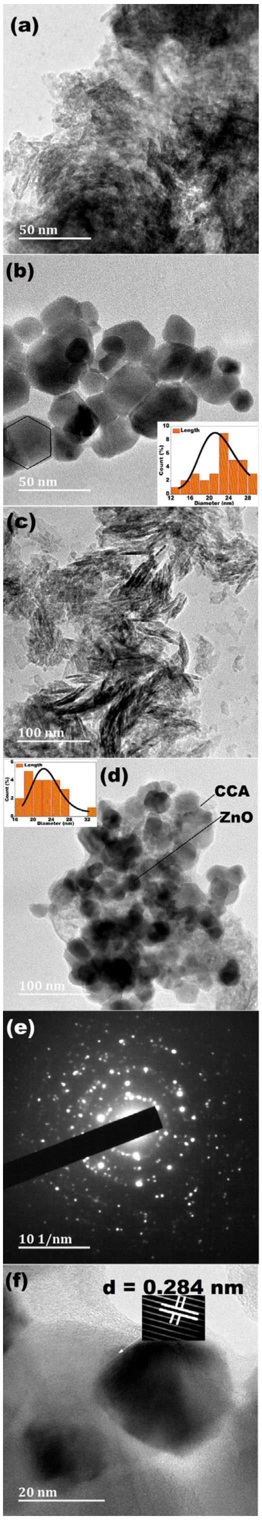

Fig. 4. TEM micrographs of (a) alumina, (b) ZnO [inset — particle distribution], (c) CCA, (d) ZnO/CCA (1:2) [inset — particle distribution], (e) SAED image, and (f) lattice fringes and d-spacing of the ZnO/CCA (1:2) nanocomposite.

ZnO/CCA (1:2) nanocomposite. It also implies successful suppression of the recombination of charge carriers necessary for effective catalyst activity.

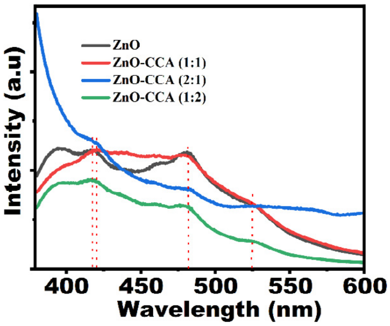

Fig. 5. PL spectra of ZnO and ZnO/CCA (various weight compositions) nanocomposites. (For interpretation of the references to colour in this figure legend, the reader is referred to the web version of this article.)

3.3.2. UV-DRS

Optical absorption data for the prepared samples was determined by UV–DRS, presented in ESI Fig. S4. Due to the influence of the CCA, the absorption edge of the ZnO/CCA composites 1:1, 1:2 and 2:1 were red-shifted to 417, 420, and 414 nm, respectively. In comparison, it was observed at 393 nm for pure ZnO. The Tauc relation $(\alpha \mathrm{h}\nu)^{\mathrm{n}} = A(\mathrm{h}\nu - \mathrm{E_g})$, where α, h, ν, and $\mathrm{E_g}$ are absorption coefficient, Planck's constant, incident photon frequency, and bandgap energy, respectively, was used to determine the value of optical absorption near the band edge for the composites. The value of n denotes the nature of the sample transition, where $n = 2$ for a direct band gap material such as ZnO and A is a constant (Ravidhas et al., 2015; Rathore et al., 2010). Hence, supplementary data ESI Fig. S4 contains the Tauc plots for all the samples. The bandgaps of ZnO, ZnO/CCA (1:1), ZnO/CCA (2:1) and ZnO/CCA (1:2) were estimated as 3.21, 3.15, 3.17 and 2.65 eV, respectively. Thus, the bandgaps of the catalysts have narrowed, leading to enhanced visible light photocatalysis (due to the ZnO and CCA) (Singh et al., 2017). The experimental results confirm the reduction in the ZnO bandgap energy (Liu et al., 2013; López and Gómez, 2012). Perhaps, the reactive functionality (Mahlambi et al., 2013) of the CCA (as a result of the carbonaceous material) leads to improved absorption of light for photocatalysis by the prepared samples (Zarrabi et al., 2019; Tahir et al., 2021). The most important factors to be considered for improving the activity of a photocatalyst are its adsorption ability, its efficiency in suppressing the rate of charge carrier recombination, and increased visible light absorption. ZnO is a well-known UV-responsive semiconductor due to its wide bandgap, also shown above; however, it is important to note that it does absorb in the visible region to a lesser extent (Lavand and Malghe, 2015).

3.4. Chemical structure

3.4.1. FTIR

The FTIR spectra of the prepared samples are presented in the ESI, Fig. S5. The spectrum of ZnO showed a strong intensity signal at circa 500 cm^{-1} and weaker bands at 687 and 1363 cm^{-1} due to the vibration of the Zn–O–Zn bond (Jayarambabu et al., 2015). The Al–O–Al absorption band at 670 cm^{-1} (Jun-Cheng et al., 2006), typical of alumina, was shifted to 667 cm^{-1} on CCA and further shifted to a longer wavenumber 671 cm^{-1} for the ZnO/CCA hybrid composite. In addition, the absorption band usually observed at 1100 cm^{-1}, also typical of alumina, due to the Al–O vibration mode (Xu et al., 2017), was shifted to 1088 cm^{-1} for CCA due to the vibration of the C–O–C bond. The characteristic bands (Jun-Cheng et al., 2006) associated with γ-alumina between 1000 cm^{-1} and 435 cm^{-1} were absent from the CCA spectrum, confirming the formation of the CCA. Compared to pure alumina, the peaks have shifted toward lower wavenumbers. The shifts denote interfacial interactions between alumina and carbon that stabilized the composite. These observations serve as further confirmation for the transformation of the alumina to CCA. Additionally, the absorption band at 2000–2400 cm^{-1} for CCA and ZnO/CCA represents the combination band of oxygen-carrying reactive groups (He et al., 2012).

In the FTIR spectrum of the ZnO/CCA (also observed in the spectra of ZnO and CCA) is a strong absorption peak at 3413 cm^{-1} (medium sharp on the CCA but broad and weak on both ZnO and ZnO/CCA), which corresponds to the stretching vibration of Al^{3+} bonded –OH species on the surface of the nanocomposites. The absorption peak at 1646 cm^{-1} seen from the spectra (sharp on CCA but broad on both ZnO and ZnO/CCA) was assigned to the bending vibration of C–OH, which may be responsible for the enhanced performance of the catalyst and the anchoring of the semiconductor nanostructures onto the CCA. Similarly, an absorption band at 495 cm^{-1} for both CCA and ZnO was shifted to a lower wavelength of 475 cm^{-1} on the ZnO/CCA spectrum, and a unique signal at 588 cm^{-1} was observed only for the ZnO/CCA sample; both indicate the successful formation of the ZnO-on-CCA composite material (Li et al., 2011; Sapkota et al., 2019; Zhang et al., 2018).

3.5. Thermal stability

Thermogravimetric analysis (TGA) was performed to assess the thermal stability of the prepared nanocomposites. Each of the ZnO/CCA nanocomposites (with varying compositions of ZnO/CCA) exhibited weight loss in four stages. The first (to 150 °C) and second (150-265 °C) weight losses of 0.23% and 0.28%, respectively signify the removal of physically adsorbed water and the loss of some organic components. Thermal degradation of physisorbed and chemisorbed carbon materials was seen as the third weight loss of 0.47% (to 470 °C). The final weight loss of 2% (rapid that began at 470 °C) was associated with the complete decomposition of all organic matter, at 686 °C. While the weight loss pattern for ZnO/CCA (1:1) is similar to the thermograms reported elsewhere (Khan et al., 2021). The data showed a general improvement in ZnO stability on the CCA support (ESI Fig. S6).

3.6. Electrochemical impedance spectroscopy (EIS) studies

The ability to transport charges across a semiconductor and its interfaces to the adsorbed species is an important factor in photocatalysis. Solid-state electrochemical impedance spectroscopy is a powerful tool for studying the electrical properties of the prepared catalytic materials. Each prepared sample displayed a depressed semi-circle with a non-Debye response at high frequencies with a diameter corresponding to the transfer resistance ($R_{\text{ct}}-$) and a linear component at low frequencies (Begum et al., 2017; Gul et al., 2019; Merlo et al., 2021; Yang et al., 2021). ESI Fig. S7 displays the Nyquist graphs of the prepared samples [ZnO, ZnO/CCA (1:1), ZnO/CCA (2:1), and ZnO/CCA (1:2)]. The ZnO/CCA (1:2) composite had the smallest diameter (incomplete circle), indicating that it has the best conductivity (smallest transfer resistance) compared to ZnO, ZnO/CCA (1:1), and ZnO/CCA (2:1). The more credible explanation may be that CCA acts as an electron sensitizer due to the variety of surface reactive groups. Similar observations have been reported (Kumar and Rao, 2015; Liu et al., 2019; Mahlambi et al., 2012, 2013).

3.7. Photocatalytic degradation study

The catalytic performance of the prepared samples was evaluated using visible light irradiation. This is one of the key objectives of this project, i.e. the exclusion of UV light for the photodegradation of the dye contaminants. In the set-up, sunset yellow (FCF) and tartrazine were used as the dye contaminants at a concentration of 20 mg/L. The adsorption–desorption and photodegradation profiles of the dyes are presented in Fig. S8 (ESI). In addition, Fig. S9 shows the time-dependent UV absorption profiles of aqueous solutions of the dyes during the degradation by ZnO/CCA (1:2) photocatalyst exposed to visible light. The photographic insets show the accompanying colour changes in the course of photolysis. The suspension was initially agitated in a dark enclosure for 30 min to equilibrate the nanocatalyst and the dye contaminant before irradiation with visible light. The ZnO/CCA samples showed higher dye adsorption than the pristine ZnO sample. This may be ascribed to the larger specific areas of the composite catalysts, hence, providing more open reactive spots for dye adsorption. As shown in ESI Fig. S8, all the prepared ZnO/CCA samples showed significant degradation of the sunset yellow and tartrazine dyes. An optimum amount of CCA is critical to ensure the support's light-gathering ability and a direct correlation is observed between photocatalytic activity and the amount of CCA in the hybrid catalyst. This is because the ZnO catalyst is locked in the pores of the CCA and available to photolyse the dye throughout the 180 min irradiation period (Huang et al., 2014; Lin et al., 2019; Solodovnichenko et al., 2019).

The activity of the catalyst on the surface adsorbed dye molecules is critical during photocatalysis. Hence a set of control experiments were conducted to determine the influence of the ZnO/CCA composite on the photocatalytic process. The results showed that only 11% of sunset yellow and 9% of tartrazine were photolysed without the catalyst. Then a set of control experiments were conducted in the dark, which indicated that the ZnO, ZnO/CCA [(1:1), (2:1), and (1:2)] catalysts, respectively adsorbed 3, 15, 17, and 25% of the sunset yellow (FCF). Also, the same catalysts removed 4, 28, 25, and 22% of tartrazine by adsorption in the dark. All adsorption measurements were completed within 30 min before the onset of dye degradation. These control results and the observations shown in Fig. S8(a, b) indicate that both visible light and a catalyst are required for effective lyses of the dye pollutants. Furthermore, the results showed that the ZnO/CCA (1:2) photocatalyst degraded about 99% of the sunset yellow (FCF) and 92% of the tartrazine dye in 180 min exposure to visible light. At the same time, ZnO/CCA (1:1) degraded the sunset yellow (FCF) by about 93% and tartrazine by 77%, which were recently studied by empirical mathematical modelling (do Nascimento et al., 2020).

Similarly, ZnO/CCA (2:1) degraded the sunset yellow (FCF) by 96% and tartrazine by about 68% within the same time. Therefore, dye removal occurred by photolysis on the ZnO/CCA nanocomposites since less than 30% of each dye was removed by adsorption for all the catalysts. It is important to emphasize that the amount of dye removed via adsorption increased with the amount of CCA incorporated into the composite. Hence, the ZnO/CCA (1:2) photocatalyst was highlighted for more detailed experimental studies. In the photocatalytic pathway, the excellent performance of the ZnO/CCA composite could be due to the embedded CCA causing structural defects that modified the property of ZnO (reduced bandgap energy) and, thus, enhancing its light absorption properties (Srinivasan et al., 2019). The photogenerated charge carrier recombination rate is also curbed in the ZnO/CCA (1:2), hence the high photoactivity. The rapid loss of colour in both azo dye solutions is linked to the cleavage of the azo linkage in the dye molecules (Table 1). The chromophore is the most easily sensitized and active bond in the dye molecule which is easily attacked by positive holes and hydroxyl

Table 3
Photocatalytic activity of the ZnO/CCA (1:2) compared with a TiO_2-based system.

Photocatalyst	Light source	Method of synthesis	Pollutant (conc.)	Degradation (%)	Degradation time (min)	Ref.
TiO_2/CCA (100 mg)	Vis	Precipitation/ Calcination	RB[a] (10 mg/L)	100	180	Mahlambi et al. (2012)
ZnO/CCA (10 mg)	Vis	Sol–gel/ Calcination	SY[b] & TA[c] (20 mg/L)	99 & 92	180	This work

[a] Rhodamin B (RB).
[b] Sunset yellow (SY).
[c] Tartrazine (TA).

radicals (Nenavathu et al., 2018). The increased photocatalytic performance may also be due to the higher specific area (110 m^2/g) for the material, which is synonymous with an increased number of available active sites. However, it must be emphasized that although surface area plays a vital role in photoactivity, other conditions like the light gathering ability of the composite (due to reactive groups on the CCA) (Sapkota et al., 2019) and better separation of photoinduced charge carriers are similarly crucial in determining photocatalytic performance (Nenavathu et al., 2018; Praveen et al., 2018). Table 3 compares the photocatalytic performance of the as-prepared nanocomposite to the activity of a titania catalyst bearing the CCA support.

3.7.1. Degradation analysis

Physico-chemical factors including the pH, colour, chemical oxygen demand (COD) and total dissolved solids (TDS) are important considerations for any effective wastewater clean-up process. The values of these parameters reflect the extent of water contamination. Destroying the chromophore (decolourization) does not translate to mineralization because numerous secondary intermediates produced during photocatalysis may pose concealed toxicity. Results of the physico-chemical analysis of the samples are presented in ESI Table S1. Solutions of the untreated sunset yellow and tartrazine dyes were characteristically coloured orange and yellow respectively. The colours cleared after treatment with the ZnO/CCA catalysts. Data for the COD test and pH monitoring showed that a reduction in pH was observed for all the treated water samples (compare entries 1–2 with 3–4, Table S1). This may result from dissolved mineral acids, an intermediate product of photocatalytic degradation of organic pollutants. For sunset yellow (FCF), after 180 min of visible light exposure with pure ZnO (entry 3) and ZnO/CCA (entry 4), the COD was reduced by 26% (to 17 mg/L) and 70% (to 7 mg/L) from 23 mg/L, respectively. While, for tartrazine, the COD reduction for pure ZnO and ZnO/CCA, are respectively 19% (to 15 mg/L) and 62% (to 7 mg/L) from 18.5 mg/L. The reduction in pH may also be due to carboxylic acids (intermediate products), which are much more difficult to break down than the azo chromophore because their oxidation proceeds at a slower rate (Bilinska et al., 2015; Ince et al., 1997; Nagarajan and Venkatanarasimhan, 2019). The results further confirm the improved mineralization potential of the ZnO/CCA system for dye removal from the water. The whitish appearance of the water samples may be due to the presence of free ZnO, as evidenced by an increase in the TDS value (401 for sunset yellow and 478 for tartrazine) of the decolourized (clean) water samples. The TDS value of the treated water measures the quantity of the nanocatalyst retained. For the ZnO/CCA nanocatalyst, TDS increases were insignificant at less than 8% for both dyes. Compared to the observed increases of 188% and 132% for ZnO as a catalyst (Table S1, entry 3). This further validates our observation that the support effectively reduced catalyst leaching during the photocatalytic study (see below). According to the TDS and COD studies, the fabricated nanomaterials were very effective photocatalysts for removing the dyes from the wastewater and further degrading any resulting toxicants. The COD results closely agree with the photodegradation results, indicating almost complete mineralization of the dye pollutants into naturally harmless products.

3.8. Photocatalytic reaction kinetics

A kinetic study on the photodegradation of the dyes was carried out to understand the process's limitations further. The data presented in Table 4 (see ESI Fig. S10 for the plots – ln (A_t/A_0) as a function of time for all the catalysts) is consistent with pseudo-first-order reaction kinetics (Wu et al., 2019). The rate constants, k for the removal of sunset yellow (FCF) by ZnO and ZnO/CCA, [(1:1), (2:1), (1:2)] catalysts are 0.0124, 0.0153, 0.0186 and 0.0219 min^{-1} respectively. While, for tartrazine, the rate constants by the same catalysts are 0.0019, 0.0049, 0.0061 and 0.0112 min^{-1}, respectively. These results are similar to those obtained for a ZnO photocatalyzed process (Wu et al., 2019). The data shows that the rate constant increased with the relative quantity of CCA in the hybrid catalysts. It is noticeable that the ZnO/CCA (1:2) catalyst photodegraded sunset yellow (FCF) and tartrazine at faster rates, twice and six times quicker than pure ZnO.

Similarly, the rate is even faster with ZnO/CCA (2:1) at 12 and 37 times quicker for the two dyes. These remarkable performances are due to the lowest bandgap exhibited by ZnO/CCA (1:2) (see Fig. S4d). In addition, the efficient separation of the photoinduced charge carriers, coupled with the higher porosity of its structure, accounted for the observed activity.

Also, embedding the ZnO onto the CCA caused fundamental alterations to the electronic band structure of the material, resulting in the observed improvements over pristine ZnO. More significantly, the carbon coating enabled cross-plane movement (diffusion channels), which improved charge and mass transfer and, as a result, increased photocatalytic efficiencies (Li et al., 2020; Lu et al., 2020; Wu et al., 2020).

Table 4
Rate constants (k) for the degradation of the dyes by the ZnO/CCA nanocomposites.

Entry	Catalyst	k (min^{-1}) SY[a] (TA)[b]	Maximum degradation (%) SY[a] (TA)[b]
1	Dye (No catalyst)	0.0018 (0.003)	11 (9)
2	ZnO	0.0124 (0.0019)	36 (31)
3	ZnO/CCA (1:1)	0.0153 (0.0049)	93 (77)
4	ZnO/CCA (2:1)	0.0186 (0.0061)	96 (68)
5	ZnO/CCA (1:2)	0.0219 (0.0112)	99 (92)

[a] Sunset yellow (SY).
[b] Tartrazine (TA).

3.9. Proposed mechanism

Radical scavenging experiments were performed to determine the reactive entities involved in dye degradation by the ZnO/CCA (1:2) photocatalyst. Scavengers for the known ($^{\cdot}OH$, h^+, and $O_2^{\cdot-}$) photoinduced radicals were introduced, and the results are presented in ESI Fig. S11(a, b).

It is noticeable that the radical scavengers, disodium ethylenediaminetetraacetic acid (EDTA) and *p*-benzoquinone (BQ), significantly diminished the activity of the ZnO/CCA (1:2) photocatalyst. A study of the various scavengers and their known modes of action points to the type of radicals involved in the photocatalytic process. The fact that higher activity reductions were observed for BQ and EDTA (see Fig. S11) indicates the involvement of h^+ (followed by $O_2^{\cdot-}$ and $^{\cdot}OH$) in the photodegradation of the two dyes.

The steps involved in a typical photocatalytic process are:

- light-harvesting and generation of photoinduced carriers;
- photoinduced charge carrier separation and transfer to catalyst surface;
- redox reaction on the surface of the catalyst.

In light of these, the effective utilization of surface electrons and holes is also crucial for photocatalytic efficiency. An illustration depicting the pathway for the ZnO/CCA photocatalyzed process is shown in ESI Fig. S12. This study has demonstrated an improvement for the ZnO semiconductor by impregnation with CCA. This is because, generally, ZnO is mainly stimulated by UV light with minimal visible light absorbance (Baruah et al., 2010; Lavand and Malghe, 2015; Senasu et al., 2021). An increase in light absorption in the visible region coupled with an improved pollutant adsorption capacity and efficient charge carrier separation are the main factors responsible for the improved performance of the photocatalysts reported herein.

The exciton (e^-/h^+ pair) produced during photocatalysis is prone to irradiative recombination, which must be hindered to make available the electron for further dye degradation reactions. The photoinduced charged pair recombination is successfully hindered if they are separated efficiently for long periods. In the illustration (Fig. S12), when ZnO/CCA (1:2) was exposed to visible light, the electron in the valence band (VB) was agitated and stimulated to the conduction band (CB), where it was easily captured by CCA, while h^+ remained in the VB. As a result, the photogenerated excitons move in opposite directions in a cyclic pathway. This phenomenon is responsible for the increase in exciton life span, which increased the number of opportunities per unit time for the photoactive species to participate in the photocatalytic reaction, resulting in increased efficiency. Typically, photoinduced electrons in the CB are scavenged by surrounding O_2 to form $O_2^{\cdot-}$, whereas h^+ in the VB reacts with H_2O to yield hydrogen ions (H^+) and hydroxyl radicals ($^{\cdot}OH$) (Bouarroudj et al., 2021). As a result, the H^+ reacts with $O_2^{\cdot-}$ to produce the $^{\cdot}OOH$ radical that is further reduced to H_2O_2, which generates the reactive OH^- and $^{\cdot}OH$ radicals (Bouarroudj et al., 2021). According to Srinivasan et al. (2019), the photogenerated reactive entities (h^+, $^{\cdot}OH$ and $O_2^{\cdot-}$) then participate in degrading the dyes to CO_2, mineral acids, and H_2O. Therefore, the improved photocatalytic performance of the ZnO/CCA (1:2) catalyst may be due to an ease in the generation of the photo-charges due to its low bandgap energy and the reduced recombination rate of the excitons (Liu et al., 2019; Merlo et al., 2021; Zhang et al., 2019).

3.10. Reusability of the ZnO/CCA (1:2) nanocomposite and its photostability

Fig. S13 presents the results of the photostability tests conducted on the most active ZnO/CCA (1:2) nanocomposite. After each cycle, the catalyst was retrieved by simple centrifugation, filtered, rinsed several times with deionized water, dried overnight at 80 °C, and reused in the next cycle. The results indicate little or no loss in catalyst performance up to the fifth cycle, with only a minimal reduction in dye degradation efficiency from 99% in the first cycle to 95% in the fifth for sunset yellow (FCF). Similarly, by the fifth cycle, photocatalytic performance for tartrazine only reduced from 92% to 84%, indicating ease of recyclability and potential for catalyst reuse.

3.11. Applications and future research prospects

Coloured organic compounds in water bodies are potentially harmful to life, and there is a growing need for sustainable methods for their removal. Heterogeneous photocatalysis is the most viable method of wastewater decontamination. This study developed a simple, cheap and sustainable route to the synthesis of modified ZnO nanocatalysts that have addressed some of the inherent shortcomings of heterogeneous photocatalysis. Key amongst which are poor visible light utilization and separation of photogenerated charges. Hence, the ZnO/CCA nanocomposites have practical applications as visible/solar light-driven photocatalysts for pre-treating effluent wastewater contaminated with organic dyes. The advantages are enormous because the process is cheap, safe and green. Immediate prospects from this work include expanding the application to an industrial scale, which will require some enhancements toward more robust CCA-supported semiconductors. These may include the development of metal-ion-doped ZnO nanomaterials and binary/ternary nanostructured materials containing ZnO supported on CCA. Also, depending on requirements, the ZnO/CCA composites may be further supported on a more rigid platform like glass or a pliable one like paper to further improve catalyst recovery and recycling at a municipal or industrial wastewater treatment scale.

4. Conclusions

The synthesis and successful incorporation of ZnO nanocatalysts onto CCA supports utilizing the reactivity of TDI groups is reported for the first time. This is a significant advancement towards using ZnO photocatalysts for environmental remediation under visible light. The as-prepared CCA combined the alumina's texture and carbon's surface chemistry. COD measurements further confirmed the complete degradation of the model pollutants. The novel photocatalysts synthesized by following a low-cost and straightforward route are expected to provide impetus to future large-scale and commercial adoption of the ZnO/CCA catalyst systems.

CRediT authorship contribution statement

Abayomi D. Folawewo: Literature collection, Data analysis, Writing – original draft, Writing – review & editing. **Muhammad D. Bala:** Supervision, Budget, Project initiation, Writing – review & editing.

Declaration of competing interest

The authors declare that they have no known competing financial interests or personal relationships that could have appeared to influence the work reported in this paper.

Data availability

I have shared the data as supplementary materials accompanying the paper.

Acknowledgements

We thank the NRF, South Africa and ESKOM, South Africa (TESP program) for financial support.

Ethical approval

No ethical approval is required for the work reported in this paper.

Appendix A. Supplementary data

Supplementary material related to this article can be found online at https://doi.org/10.1016/j.eti.2022.102866.

References

Afzaal, M., Malik, M.A., O'Brien, P., 2007. Preparation of zinc containing materials. New J. Chem. 31, 2029–2040. http://dx.doi.org/10.1039/b712235g.

Ajmal, A., Majeed, I., Malik, R.N., Idriss, H., Nadeem, M.A., 2014. Principles and mechanisms of photocatalytic dye degradation on TiO_2 based photocatalysts: A comparative overview. RSC Adv. 4, 37003–37026. http://dx.doi.org/10.1039/C4RA06658H.

Baruah, S., Mahmood, M.A., Myint, M.T.Z., Bora, T., Dutta, J., 2010. Enhanced visible light photocatalysis through fast crystallization of zinc oxide nanorods. Beilstein J. Nanotechnol. 1, 14–20. http://dx.doi.org/10.3762/bjnano.1.3.

Begum, H., Ahmed, M.S., Jeon, S., 2017. New approach for porous chitosan–graphene matrix preparation through enhanced amidation for synergic detection of dopamine and uric acid. ACS Omega 2, 3043–3054. http://dx.doi.org/10.1021/acsomega.7b00331.

Behnajady, M.A., Modirshahla, N., Ghazalian, E., 2011. Synthesis of ZnO nanoparticles at different conditions: A comparison of photocatalytic activity. Dig. J. Nanomater. Biostructures 6, 467–474.

Bekele, B., Jule, L.T., Saka, A., 2021. The effects of annealing temperature on size, shape, structure and optical properties of synthesized zinc oxide nanoparticles by sol–gel methods. Dig. J. Nanomater. Biostructures 16, 471–478.

Bilinska, L., Gmurek, M., Ledakowicz, S., 2015. Application of advanced oxidation technologies for decolourization and mineralization of textile wastewaters. J. Adv. Oxid. Technol. 18, 185–194. http://dx.doi.org/10.1515/jaots-2015-0202.

Bond, T.C., Bergstrom, R.W., 2006. Light absorption by carbonaceous particles: An investigative review. Aerosol Sci. Technol. 40, 27–67. http://dx.doi.org/10.1080/02786820500421521.

Boorman, P., Chong, K., Kydd, R., Lewis, J., 1991. A comparison of alumina, carbon, and carbon-covered alumina as supports for Ni-Mo-F additives - carbon deposition and model-compound reaction studies. J. Catalysis 128, 537–550. http://dx.doi.org/10.1016/0021-9517(91)90311-q.

Bouarroudj, T., Aoudjit, L., Djahida, L., Zaidi, B., Ouraghi, M., Zioui, D., Mahidine, S., Shekhar, C., Bachari, K., 2021. Photodegradation of tartrazine dye favoured by natural sunlight on pure and (Ce, Ag) co-doped ZnO catalysts. Water Sci. Technol. 83, 2118–2134. http://dx.doi.org/10.2166/wst.2021.106.

Caliman, F., Apostol, L., Hlihor, R., Gavrilescu, M., 2008. Factors influencing the sorption of anionic azo dye tartrazine from aqueous solutions onto natural clay. Materiale Si Procese Inovative 455–460.

Chen, X., Wu, Z., Liu, D., Gao, Z., 2017. Preparation of ZnO photocatalyst for the efficient and rapid photocatalytic degradation of azo dyes. Nanoscale Res. Lett. 12, 143. http://dx.doi.org/10.1186/s11671-017-1904-4.

Crini, G., 2006. Non-conventional low-cost adsorbents for dye removal: A review. Bioresour. Technol. 97, 1061–1085. http://dx.doi.org/10.1016/j.biortech.2005.05.001.

Dixit, S., Yadav, A., Dwivedi, P.D., Das, M., 2015. Toxic hazards of leather industry and technologies to combat threat: A review. J. Clean. Prod. 87, 39–49. http://dx.doi.org/10.1016/j.jclepro.2014.10.017.

González-Casamachin, D.A., De la Rosa, J.R., Lucio-Ortiz, C.J., De Rio, D.A.D.H., Martínez-Vargas, D.X., Flores-Escamilla, G.A., Guzman, N.E.D., Ovando-Medina, V.M., Moctezuma-Velazquez, E., 2019. Visible light photocatalytic degradation of acid violet 7 dye in a continuous annular reactor using ZnO/PPy photocatalyst: Synthesis, characterization, mass transfer effect evaluation and kinetic analysis. Chem. Eng. J. 373, 325–337. http://dx.doi.org/10.1016/j.cej.2019.05.032.

Gul, H., Shah, A.U.H.A., Bilal, S., 2019. Achieving ultrahigh cycling stability and extended potential window for supercapacitors through asymmetric combination of conductive polymer nanocomposite and activated carbon. Polymers 11, 1678. http://dx.doi.org/10.3390/polym11101678.

Hasanbeigi, A., Price, L., 2015. A technical review of emerging technologies for energy and water efficiency and pollution reduction in the textile industry. J. Clean Prod. 95, 30–44. http://dx.doi.org/10.1016/j.jclepro.2015.02.079.

He, Y., Zhang, X., Zhang, X., Huang, H., Chang, J., Chen, H., 2012. Structural investigations of toluene diisocyanate (TDI) and trimethylolpropane (TMP)-based polyurethane prepolymer. J. Ind. Eng. Chem. 18, 1620–1627. http://dx.doi.org/10.1016/j.jiec.2012.02.023.

Hu, J., Bando, Y., 2003. Growth and optical properties of single-crystal tubular ZnO whiskers. Appl. Phys. Lett. 82, 1401–1403. http://dx.doi.org/10.1063/1.1558899.

Huang, Z.-F., Pan, L., Zou, J.-J., Zhang, X., Wang, L., 2014. Nanostructured bismuth vanadate-based materials for solar-energy-driven water oxidation: A review on recent progress. Nanoscale 6, 14044–14063. http://dx.doi.org/10.1039/C4NR05245E.

Idriss, H., Moussa, S.A., Alaamer, A.S., Al-Rajhi, M.A., 2017. A facile and economical method for mass production of ZnO nanopowder. Dig. J. Nanomat. Biostructures 12, 1069–1073.

Ince, N.H., Stefan, M.I., Bolton, J.R., 1997. UV/H_2O_2 degradation and toxicity reduction of textile azo dyes: Remazol black-B, a case study. J. Adv. Oxid. Technol. 2, 442–448. http://dx.doi.org/10.1515/jaots-1997-0312.

Ischenko, V., Polarz, S., Grote, D., Stavarache, V., Fink, K., Driess, M., 2005. Zinc oxide nanoparticles with defects. Adv. Funct. Mater. 15, 1945–1954. http://dx.doi.org/10.1002/adfm.200500087.

Jana, P., Ganesan, V., 2011. The production of a carbon-coated alumina foam. Carbon 49, 3292–3298. http://dx.doi.org/10.1016/j.carbon.2011.04.005.

Jayarambabu, N., Kumari, B.S., Rao, K.V., Prabhu, Y.T., 2015. Beneficial role of zinc oxide nanoparticles on green crop production. Int. J. Multidiscip. Adv. Res. Trends 2, 273–282.

Jun-Cheng, L., Lan, X., Feng, X., Zhan-Wen, W., Fei, W., 2006. Effect of hydrothermal treatment on the acidity distribution of γ-Al_2o_3 support. Appl. Surf. Sci. 253, 766–770. http://dx.doi.org/10.1016/j.apsusc.2006.01.003.

Kandula, S., Jeevanandam, P., 2014. Visible-light-induced photodegradation of methylene blue using ZnO/CdS heteronanostructures synthesized through a novel thermal decomposition approach. J. Nanopart. Res. 16, 1–18. http://dx.doi.org/10.1007/s11051-014-2452-9.

Kazakova, M.A., Vatutina, Y.V., Prosvirin, I.P., Gerasimov, E.Y., Shuvaev, A.V., Klimov, O.V., Noskov, A.S., Kazakov, M.O., 2021. Boosting hydrodesulfurization activity of $CoMo/Al_2O_3$ catalyst via selective graphitization of alumina surface. Microporous Mesoporous Mater. 317, 111008-111020. http://dx.doi.org/10.1016/j.micromeso.2021.111008.

Khan, M., Ware, P., Shimpi, N., 2021. Synthesis of ZnO nanoparticles using peels of passiflora foetida and study of its activity as an efficient catalyst for the degradation of hazardous organic dye. SN Appl. Sci. 3, 1–17. http://dx.doi.org/10.1007/s42452-021-04436-4.

Konstantinou, I.K., Albanis, T.A., 2004. TiO_2-assisted photocatalytic degradation of azo dyes in aqueous solution: Kinetic and mechanistic investigations: A review. Appl. Catal. B 49, 1–14. http://dx.doi.org/10.1016/j.apcatb.2003.11.010.

Kumar, S.G., Rao, K.K., 2015. Zinc oxide based photocatalysis: Tailoring surface-bulk structure and related interfacial charge carrier dynamics for better environmental applications. RSC Adv. 5, 3306–3351. http://dx.doi.org/10.1039/C4RA13299H.

Landers, J., Gor, G.Y., Neimark, A.V., 2013. Density functional theory methods for characterization of porous materials. Colloids Surf. A 437, 3–32. http://dx.doi.org/10.1016/j.colsurfa.2013.01.007.

Lavand, A.B., Malghe, Y.S., 2015. Visible light photocatalytic degradation of 4-chlorophenol using C/ZnO/CdS nanocomposite. J. Saudi Chem. Soc. 19, 471–478. http://dx.doi.org/10.1016/j.jscs.2015.07.001.

Legrand, U., Klassen, D., Watson, S., Aufoujal, A., Nisol, B., Boudreault, R., Waters, K.E., Meunier, J.L., Girard-Lauriault, P.L., Wertheimer, M.R., Tavares, J.R., 2021. Nanoporous sponges as carbon-based sorbents for atmospheric water generation. Ind. Eng. Chem. Res. 60, 12923–12933. http://dx.doi.org/10.1021/acs.iecr.1c02248.

Li, X., Qin, Y., Picraux, S.T., Guo, Z.X., 2011. Noncovalent assembly of carbon nanotube-inorganic hybrids. J. Mater. Chem. 21, 7527–7547. http://dx.doi.org/10.1039/c1jm10516g.

Li, M., Wu, G., Liu, Z., Xi, X., Xia, Y., Ning, J., Yang, D., Dong, A., 2020. Uniformly coating ZnAl layered double oxide nanosheets with ultra-thin carbon by ligand and phase transformation for enhanced adsorption of anionic pollutants. J. Hazard. Mater. 397, 122766-122766. http://dx.doi.org/10.1016/j.jhazmat.2020.122766.

Lin, B., Heng, L., Yin, H., Fang, B., Ni, J., Wang, X., Lin, J., Jiang, L., 2019. Effects of using carbon-coated alumina as support for Ba-promoted Ru catalyst in ammonia synthesis. Ind. Eng. Chem. Res. 58, 10285–10295. http://dx.doi.org/10.1021/acs.iecr.9b01610.

Lin, L., Lin, W., Zhu, Y.X., Zhao, B.Y., Xie, Y.C., Jia, G.Q., Li, C., 2005. Uniformly carbon-covered alumina and its surface characteristics. Langmuir 21, 5040–5046. http://dx.doi.org/10.1021/la047097d.

Liu, Y.J., 2011. Characterization of spent catalysts during hydrodemetallization of atmosphere residue. Adv. Mater. Res. 236, 538–542. http://dx.doi.org/10.4028/www.scientific.net/AMR.236-238.538.

Liu, J.-Y., Bai, Y., Luo, P.-Y., Wang, P.-Q., 2013. One-pot synthesis of graphene–BiOBr nanosheets composite for enhanced photocatalytic generation of reactive oxygen species. Catal. Commun. 42, 58–61. http://dx.doi.org/10.1016/j.catcom.2013.07.043.

Liu, C., Bao, L., Yang, M., Zhang, S., Zhou, M., Tang, B., Wang, B., Liu, Y., Zhang, Z.L., Zhang, B., Pang, D.W., 2019. Surface sensitive photoluminescence of carbon nanodots: Coupling between the carbonyl group and π-electron system. J. Phys. Chem. Lett. 10, http://dx.doi.org/10.1021/acs.jpclett.9b01339, 3621-362.

López, R., Gómez, R., 2012. Band-gap energy estimation from diffuse reflectance measurements on sol–gel and commercial TiO_2: A comparative study. J. Sol-Gel Sci. Technol. 61, 1–7. http://dx.doi.org/10.1007/s10971-011-2582-9.

Lu, K., Li, B., Zhan, X., Xia, F., Dahunsi, O.J., Gao, S., Reed, D.M., Sprenkle, V.L., Li, G., Cheng, Y., 2020. Elastic Na_xMoS_2-carbon-BASE triple interface direct robust solid–solid interface for all-solid-state Na–S batteries. Nano Lett. 20, 6837–6844. http://dx.doi.org/10.1063/1.3466543.

Mahlambi, M.M., Mishra, A.K., Mishra, S.B., Krause, R.W., Mamba, B.B., Raichur, A.M., 2012. Synthesis and characterization of carbon-covered alumina (CCA) supported TiO_2 nanocatalysts with enhanced visible-light photodegradation of Rhodamine B. In: Nanotechnology for Sustainable Development. Springer, Chem, pp. 89–99.

Mahlambi, M.M., Mishra, A.K., Mishra, S.B., Krause, R.W., Mamba, B.B., Raichur, A.M., 2013. Effect of metal ions (Ag, Co, Ni, and Pd) on the visible light degradation of Rhodamine B by carbon-covered alumina-supported TiO_2 in aqueous solutions. Ind. Eng. Chem. Res. 52, 1783–1794. http://dx.doi.org/10.1021/ie3025505.

Maity, S., Flores, L., Ancheyta, J., Fukuyama, H., 2009. Carbon-modified alumina and alumina- carbon-supported hydrotreating catalysts. Ind. Eng. Chem. Res. 48, 1190–1195. http://dx.doi.org/10.1021/ie800606p.

Masthan, S.K., Prasad, P.S., Rao, K.R., Rao, P.K., 1991. Hysteresis during ammonia synthesis over promoted ruthenium catalysts supported on carbon-covered alumina. J. Mol. Catal. 67, L1–L5. http://dx.doi.org/10.1016/0304-5102(91)85040-9.

Mendes, F.L., da Silva, V.T., Pacheco, M.E., de Rezende Pinho, A., Henriques, C.A., 2020. Hydrotreating of fast pyrolysis oil: A comparison of carbons and carbon-covered alumina as supports for Ni_2P. Fuel 264, 116764-116764. http://dx.doi.org/10.1016/j.fuel.2019.116764.

Merlo, M.A., Jaimes, D.A., Escrig, J., Pérez, O.L., Bajales, N., 2021. Carbon-coated alumina nanochannels-based composite: A conductivity analysis by means of electrochemical impedance spectroscopy. Mater. Lett. 295, 129795-129795. http://dx.doi.org/10.1016/j.matlet.2021.129795.

Monson, P.A., 2012. Understanding adsorption/desorption hysteresis for fluids in mesoporous materials using simple molecular models and classical density functional theory. Microporous Mesoporous Mater. 160, 47–66. http://dx.doi.org/10.1016/j.micromeso.2012.04.043.

Moradi, M., Haghighi, M., Allahyari, S., 2017. Precipitation dispersion of Ag–ZnO nanocatalyst over functionalized multiwall carbon nanotube used in degradation of acid orange from wastewater. Process Saf. Environ. Prot. 107, 414–427. http://dx.doi.org/10.1016/j.psep.2017.03.010.

Morshed, M.N., Bouazizi, N., Behary, N., Guan, J., Nierstrasz, V., 2019. Stabilization of zero valent iron (Fe^0) on plasma/dendrimer functionalized polyester fabrics for fenton-like removal of hazardous water pollutants. Chem. Eng. J. 374, 658–673. http://dx.doi.org/10.1016/j.cej.2019.05.162.

Nadupalli, S., Repp, S., Weber, S., Erdem, E., 2021. About defect phenomena in ZnO nanocrystals. Nanoscale 13, 9160–9171. http://dx.doi.org/10.1039/D1NR00943E.

Nagarajan, D., Venkatanarasimhan, S., 2019. Copper (II) oxide nanoparticles coated cellulose sponge—an effective heterogeneous catalyst for the reduction of toxic organic dyes. Environ. Sci. Pollut. Res. 26, 22958–22970. http://dx.doi.org/10.1007/s11356-019-05419-0.

do Nascimento, G.E., Cavalcanti, V.O.M., Santana, R.M.R., Sales, D.C.S., Rodríguez-Díaz, J.M., Napoleão, D.C., Duarte, M.M.M.B., 2020. Degradation of a sunset yellow and tartrazine dye mixture: Optimization using statistical design and empirical mathematical modelling. Water Air Soil Pollut. 231, 1–17. http://dx.doi.org/10.1007/s11270-020-04547-5.

Nenavathu, B.P., Kandula, S., Verma, S., 2018. Visible-light-driven photocatalytic degradation of safranin-t dye using functionalized graphene oxide nanosheet (FGS)/ZnO nanocomposites. RSC Adv. 8, 19659–19667. http://dx.doi.org/10.1039/c8ra02237b.

Nishikiori, H., Sato, T., Kubota, S., Tanaka, N., Shimizu, Y., Fujii, T., 2012. Preparation of Cu-doped TiO_2 via refluxing of alkoxide solution and its photocatalytic properties. Res. Chem. Intermed. 38, 595–613. http://dx.doi.org/10.1007/s11164-011-0374-z.

Ong, C.B., Mohammad, A.W., Rohani, R., Ba-Abbad, M.M., Hairom, N.H.H., 2016. Solar photocatalytic degradation of hazardous congo red using low-temperature synthesis of zinc oxide nanoparticles. Process Saf. Environ. Prot. 104, 549–557. http://dx.doi.org/10.1016/j.psep.2016.04.006.

Oprea, O., Andronescu, E., Vasile, B.S., Voicu, G., Covaliu, C., 2011. Synthesis and characterization of ZnO nanopowder by non-basic route. Dig. J. Nanomater. Biostructures 6, 1393–1401.

Perez-Urquiza, M., Beltran, J., 2000. Determination of dyes in foodstuffs by capillary zone electrophoresis. J. Chromatogr. A 898, 271–275. http://dx.doi.org/10.1016/S0021-9673(00)00841-4.

Praveen, R., Chandreshia, C.B., Ramaraj, R., 2018. Silicate sol–gel matrix stabilized ZnO-Ag nanocomposites materials and their environmental remediation applications. J. Environ. Chem. Eng. 6, 3702–3708. http://dx.doi.org/10.1016/j.jece.2017.01.048.

Quraishi, I.A., Pawar, R.A., Shinde, D.R., Chaskar, M.G., 2020. Parametric study on photocatalytic dye degradation under visible light in a flat slurry reactor with nano-ZnO photocatalyst. Mater. Today: Proc. 23, 410–422. http://dx.doi.org/10.1016/j.matpr.2020.02.061.

Ranau, R., Steinhart, H., 2004. Identification and evaluation of volatile odour-active pollutants from different odour emission sources in the food industry. Eur. Food Res. Technol. 220, 226–231. http://dx.doi.org/10.1007/s00217-004-1073-4.

Rathore, K.S., Patidar, D., Choudhary, D.N., Saxena, S., Sharma, K., 2010. Cadmium sulphide nanocrystallites: Synthesis, optical and electrical studies. Amer. Inst. Phys. Proc. 1249, 145–148. http://dx.doi.org/10.1063/1.3466543.

Ravidhas, C., Josephine, A.J., Sudhagar, P., Devadoss, A., Terashima, C., Nakata, K., Fujishima, A., Raj, A.M.E., Sanjeeviraja, C., 2015. Facile synthesis of nanostructured monoclinic bismuth vanadate by a co-precipitation method: Structural, optical and photocatalytic properties. Mater. Sci. Semicond. Process. 30, 343–351. http://dx.doi.org/10.1016/j.mssp.2014.10.026.

Ribut, S.H., Abdullah, C.A.C., Mustafa, M., Yusoff, M.Z.M., Azman, S.N.A., 2018. Influence of pH variations on zinc oxide nanoparticles and their antibacterial activity. Mater. Res. Express. 6, 025016. http://dx.doi.org/10.1088/2053-1591/aaecbc.

Sapkota, K.P., Lee, I., Hanif, M.A., Islam, M.A., Hahn, J.R., 2019. Solar-light-driven efficient ZnO–single-walled carbon nanotube photocatalyst for the degradation of a persistent water pollutant organic dye. Catalysts 9, 498. http://dx.doi.org/10.3390/catal9060498.

Sarmah, K., Roy, U.K., Maji, T.K., Pratihar, S., 2018. Role of metal exchange toward the morphology and photocatalytic activity of Cu/Ag/Au-doped ZnO: A study with a zinc-sodium acetate complex as the precursor. ACS Appl. Nano Mater. 1, 2049–2056. http://dx.doi.org/10.1021/acsanm.8b00436.

Senasu, T., Chankhanittha, T., Hemavibool, K., Nanan, S., 2021. Visible-light-responsive photocatalyst based on ZnO/CdS nanocomposite for photodegradation of reactive red azo dye and ofloxacin antibiotic. Mater. Sci. Semicond. Process. 123, 105558-105558. http://dx.doi.org/10.1016/j.mssp.2020.105558.

Serrà, A., Zhang, Y., Sepúlveda, B., Gómez, E., Nogués, J., Michler, J., Philippe, L., 2019. Highly active ZnO-based biomimetic fern-like microleaves for photocatalytic water decontamination using sunlight. Appl. Catal. B 248, 129–146. http://dx.doi.org/10.1016/j.apcatb.2019.02.017.

Sharanda, L.F., Plyuto, Y.V., Babich, I.V., Plyuto, I.V., Shpak, A.P., Stoch, J., Moulijn, J.A., 2006. Synthesis and characterization of hybrid carbon-alumina support. Appl. Surf. Sci. 252, 8549–8556. http://dx.doi.org/10.1016/j.apsusc.2005.11.078.

Shashikala, V., Kumar, V.S., Padmasri, A., Raju, B.D., Mohan, S.V., Sarma, P.N., Rao, K.R., 2007. Advantages of nano-silver-carbon covered alumina catalyst prepared by electrochemical method for drinking water purification. J. Mol. Catal. A: Chemical 268, 95–100. http://dx.doi.org/10.1016/j.molcata.2006.10.019.

Sing, K.S., 1985. Reporting physisorption data for gas/solid systems with special reference to the determination of surface area and porosity (Recommendations 1984). Pure Appl. Chem. 57, 603–619. http://dx.doi.org/10.1351/pac198557040603.

Singh, S., Sharma, R., Mehta, B.R., 2017. Enhanced surface area, high Zn interstitial defects and band gap reduction in N-doped ZnO nanosheets coupled with $BiVO_4$ leads to improved photocatalytic performance. Appl. Surf. Sci. 411, 321–330. http://dx.doi.org/10.1016/j.apsusc.2017.03.189.

Solodovnichenko, V.S., Simunin, M.M., Lebedev, D.V., Voronin, A.S., Emelianov, A.V., Mikhlin, Y.L., Parfenov, V.A., Ryzhkov, I.I., 2019. Coupled thermal analysis of carbon layers deposited on alumina nanofibres. Thermochim. Acta 675, 164–171. http://dx.doi.org/10.1016/j.tca.2019.02.012.

Souza Macedo, L., Teixeira da Silva, V., Bitter, J.H., 2019. Activated carbon, carbon nanofibers and carbon-covered alumina as support for W_2C in stearic acid hydrodeoxygenation. ChemEngineering 3, 24. http://dx.doi.org/10.3390/chemengineering3010024.

Srinivasan, N., Anbuchezhiyan, M., Harish, S., Ponnusamy, S., 2019. Hydrothermal synthesis of C doped ZnO nanoparticles coupled with $BiVO_4$ and their photocatalytic performance under the visible light irradiation. Appl. Surf. Sci. 494, 771–782. http://dx.doi.org/10.1016/j.apsusc.2019.07.093.

Sun, X., Cheng, C., Shen, J., Liu, Y., Wang, T., Ma, Q., Fan, R., 2020. Fine-tuning of negative permittivity behaviour in amorphous carbon/alumina metacomposites. Ceram. Int. 46, 8942–8948. http://dx.doi.org/10.1016/j.ceramint.2019.12.1401.

Tahir, D., Ilyas, S., Rahmat, R., Heryanto, H., Fahri, A.N., Rahmi, M.H., Abdullah, B., Hong, C.C., Kang, H.J., 2021. Enhanced visible-light absorption of Fe_2O_3 covered by activated carbon for multifunctional purposes: Tuning the structural, electronic, optical, and magnetic properties. ACS Omega 6, 28334–28346. http://dx.doi.org/10.1021/acsomega.1c04526.

Thommes, M., Kaneko, K., Neimark, A.V., Olivier, J.P., Rodriguez-Reinoso, F., Rouquerol, J., Sing, K.S., 2015. Physisorption of gases, with special reference to the evaluation of surface area and pore size distribution (IUPAC technical report). Pure Appl. Chem. 87, 1051–1069. http://dx.doi.org/10.1515/pac-2014-1117.

Wang, Y., Lau, S.P., Zhang, X., Hng, H., Lee, H., Yu, S.F., Tay, B., 2003. Enhancement of near-band-edge photoluminescence from ZnO films by face-to-face annealing. J. Cryst. Growth 259, 335–342. http://dx.doi.org/10.1016/j.jcrysgro.2003.07.015.

Wróbel, D., Boguta, A., Ion, R.M., 2001. Mixtures of synthetic organic dyes in a photoelectrochemical cell. J. PhotoChem. Photobiol. A 138, 7–22. http://dx.doi.org/10.1016/S1010-6030(00)00377-4.

Wu, Z., Chen, X., Liu, X., Yang, X., Yang, Y., 2019. A ternary magnetic recyclable $ZnO/Fe_3o_4/gC_3N_4$ composite photocatalyst for efficient photodegradation of monoazo dye. Nanoscale Res. Lett. 14, 147. http://dx.doi.org/10.1186/s11671-019-2974-2.

Wu, M., Sun, M., Zhou, H., Ma, J.Y., Ma, T., 2020. Carbon counter electrodes in dye-sensitized and perovskite solar cells. Adv. Funct. Mater. 30, 1906451–1906451. http://dx.doi.org/10.1002/adfm.201906451.

Xu, B., Yang, Y., Xu, Y., Han, B., Wang, Y., Liu, X., Yan, Z., 2017. Synthesis and characterization of mesoporous Si-modified alumina with high thermal stability. Microporous Mesoporous Mater. 238, 84–89. http://dx.doi.org/10.1016/j.micromeso.2016.02.031.

Xue, J., Ma, S., Zhou, Y., Zhang, Z., 2015. Facile synthesis of ZnO–C nanocomposites with enhanced photocatalytic activity. New J. Chem. 39, 1852–1857. http://dx.doi.org/10.1039/C4NJ02004A.

Yang, L., Lin, Y., Jia, J., Xiao, X., Li, X., Zhou, X., 2008. Light-harvesting enhancement for dye-sensitized solar cells by novel anode containing cauliflower-like TiO_2 spheres. J. Power Sources 182, 370–376. http://dx.doi.org/10.1016/j.jpowsour.2008.03.013.

Yang, X., Tian, J., Guo, Y., Teng, M., Liu, H., Li, T., Lv, P., Wang, X., 2021. ZnO nano-rod arrays synthesized with exposed {0001} facets and the investigation of photocatalytic activity. Crystals 11, 522. http://dx.doi.org/10.3390/cryst11050522.

Zarrabi, M., Haghighi, M., Alizadeh, R., Mahboob, S., 2019. Solar-light-driven photodegradation of organic dyes on sono-dispersed ZnO nanoparticles over graphene oxide: Sono vs. conventional catalyst design. Sep. Purif. Technol. 211, 738–752. http://dx.doi.org/10.1016/j.seppur.2018.10.026.

Zhang, G., Chen, D., Li, N., Xu, Q., Li, H., He, J., Lu, J., 2019. Fabrication of Bi_2MoO_6/ZnO hierarchical heterostructures with enhanced visible-light photocatalytic activity. Appl. Catal. B 250, 313–324. http://dx.doi.org/10.1016/j.apcatb.2019.03.055.

Zhang, H., Wang, X., Li, N., Xia, J., Meng, Q., Ding, J., Lu, J., 2018. Synthesis and characterization of TiO_2/graphene oxide nanocomposites for photoreduction of heavy metal ions in reverse osmosis concentrate. RSC Adv. 8, 34241–34251. http://dx.doi.org/10.1039/C8RA06681G.

Zheng, M., Shu, Y., Sun, J., Zhang, T., 2008. Carbon-covered alumina: A superior support of noble metal-like catalysts for hydrazine decomposition. Catal. Lett. 121, 90–96. http://dx.doi.org/10.1007/s10562-007-9300-9.

Zhou, W.D., Wu, X., Zhang, Y.C., Zhang, M., 2007. Solvothermal synthesis of hexagonal ZnO nanorods and their photoluminescence properties. Mater. Lett. 61, 2054–2057. http://dx.doi.org/10.1016/j.matlet.2006.08.014.